Supporting information

Chemistry, Applications, and Future Prospects of Structured Liquids

Ahmadreza Ghaffarkhah [1,2], Seyyed Alireza Hashemi [2], Ali Akbar Isari[2], Mahyar Panahi-Sarmad [1,3], Feng Jiang [3], Thomas P. Russell [4,5,6], Orlando J. Rojas [1], and Mohammad Arjmand [2*]*

[1] Bioproducts Institute, Department of Chemical & Biological Engineering, Department of Chemistry and Department of Wood Science, 2360 East Mall, The University of British Columbia, Vancouver, BC V6T 1Z3, Canada

[2] Nanomaterials and Polymer Nanocomposites Laboratory, School of Engineering, University of British Columbia, Kelowna, BC, V1V 1V7, Canada

[3] Sustainable Functional Biomaterials Laboratory, Bioproducts Institute, Department of Wood Science, The University of British Columbia, Vancouver V6T 1Z4, Canada

[4] Polymer Science and Engineering Department, University of Massachusetts Amherst, 120 Governors Drive, Amherst, MA, 01003, USA

[5] Materials Sciences Division, Lawrence Berkeley National Laboratory, 1 Cyclotron Road, Berkeley, CA, 94720, USA

[6] Advanced Institute for Materials Research (WPI-AIMR), Tohoku University, 2-1-1 Katahira, Aoba, Sendai 980-8577, Japan

***Corresponding Author:** orlando.rojas@ubc.ca; mohammad.arjmand@ubc.ca

Table S1: A complete list of abbreviations.

2-MI	2-methylimidazole
APEGs	Attractive Pickering emulsion gels
AFM	Atomic force microscopy
Alg-β-CD	Alginate-modified β-cyclodextrin
Au nanoparticles	Gold nanoparticles
Bijels	Bicontinuous interfacially jammed emulsion gels
BNC	Bacterial nanocellulose
C_{16}TAB	Hexadecyltrimethylammonium bromide
CB[8]	Cucurbit[8]uril
CdSe	Cadmium selenide
CEL-C_6	Cello-oligosaccharides with hexyl groups
Cell-C8	N-octyl cello-oligosaccharide
CR	Congo red
CNC-OSO_3H	Sulfate-functionalized cellulose nanocrystals
CNCs	Cellulose nanocrystals
CNF	Cellulose nanofiber
CTAB	Cetyltrimethylammonium bromide
CTA^+	Cetyltrimethylammonium cations
DCE	1,2-dichloroethane
DDAB	Didodecyldimethylammonium bromide
DEP	Diethylphthalate
DTBE	2,2′-dithiobis[1-(2-bromo-2-methylpropionyloxy)ethane]
F-decalin	Perfluorodecaline
FC-PLLA	Ferrocene-terminated PLLA

$FeCl_3$	Ferric chloride
$Fe(SCN)_3$	Ferric thiocyanate
Fc-PLLA	Ferrocene-terminated PLLA
FML	Ferromagnetic liquid
GOD	Glucose oxidase
GO	Graphene oxide
H_2O_2	Hydrogen peroxide
H_6TPPS	5,10,15,20-tetrakis(4-sulfonatophenyl)porphyrin
HDA	Hexanediol diacrylate
ISR	Interfacial stress rheometer
IFT	Interfacial tension
KSCN	Potassium thiocyanate
LCST	Lower critical solution temperature
LiTFSI	Bis(trifluoromethane) sulfonimidelithium salt
MA	Mellitic acid
MnH_4TPPS	5,10,15,20-tetrakis(4-sulfonatophenyl)-21H,23H-porphine manganese(III) chloride
MV	Methyl viologen
MV^{2+}	Oxidized form of methyl viologen
Np-Trx	Donor monomer consists of planar truxene (Trx) spacer with three 6-methoxynaphthalene (Np)
NPSs	Nanoparticle surfactants
ODA	Octadecyl amine
OPDA	o-phenylenediamine
P[5]AA	Pillar[5]arene carboxylic acid
PEDOT:PSS	Poly(3,4-ethylenedioxythiophene):poly(styrenesulfonate)
PEG	Polyethylene glycol
PEG-DA	Poly(ethylene glycol) diacrylate
PNIPAM	Poly(N-isopropylacrylamide)

PNIPMAM	Poly(N-isopropyl methacrylamide)
POSS-$NHC_2H_4NH_2$	Aminoethylaminopropyl isobutyl polyhedral oligomeric silsesquioxane
POSS-NH_2	Aminopropylsobutyl polyhedral oligomeric silsesquioxane
PS-Fc^+	Ferrocenium-terminated polystyrene
PS-NH_2	Amine terminated polystyrene
PS-NH_3^+	Protonated amine-terminated polystyrene
PVA	Polyvinyl alcohol
PVDF	Polyvinylidene fluoride
SAXS	Small-angle X-ray scattering
SEM	Scanning electron microscopy
SFE	Stress fitting elastometry
SPS	Supramolecular polymer surfactant
STRIPS	Solvent transfer-induced phase separation
TEM	Transmission electron microscopy
TOPO	Tri-n-octylphosphine oxide
UCST	Upper critical solution temperature
WAXS	Wide-angle X-ray scattering
XPCS	X-ray photon correlation spectroscopy
GISAXS	Grazing-incidence small-angle X-ray scattering
GIS-XPCS	Grazing incidence small angle XPCS

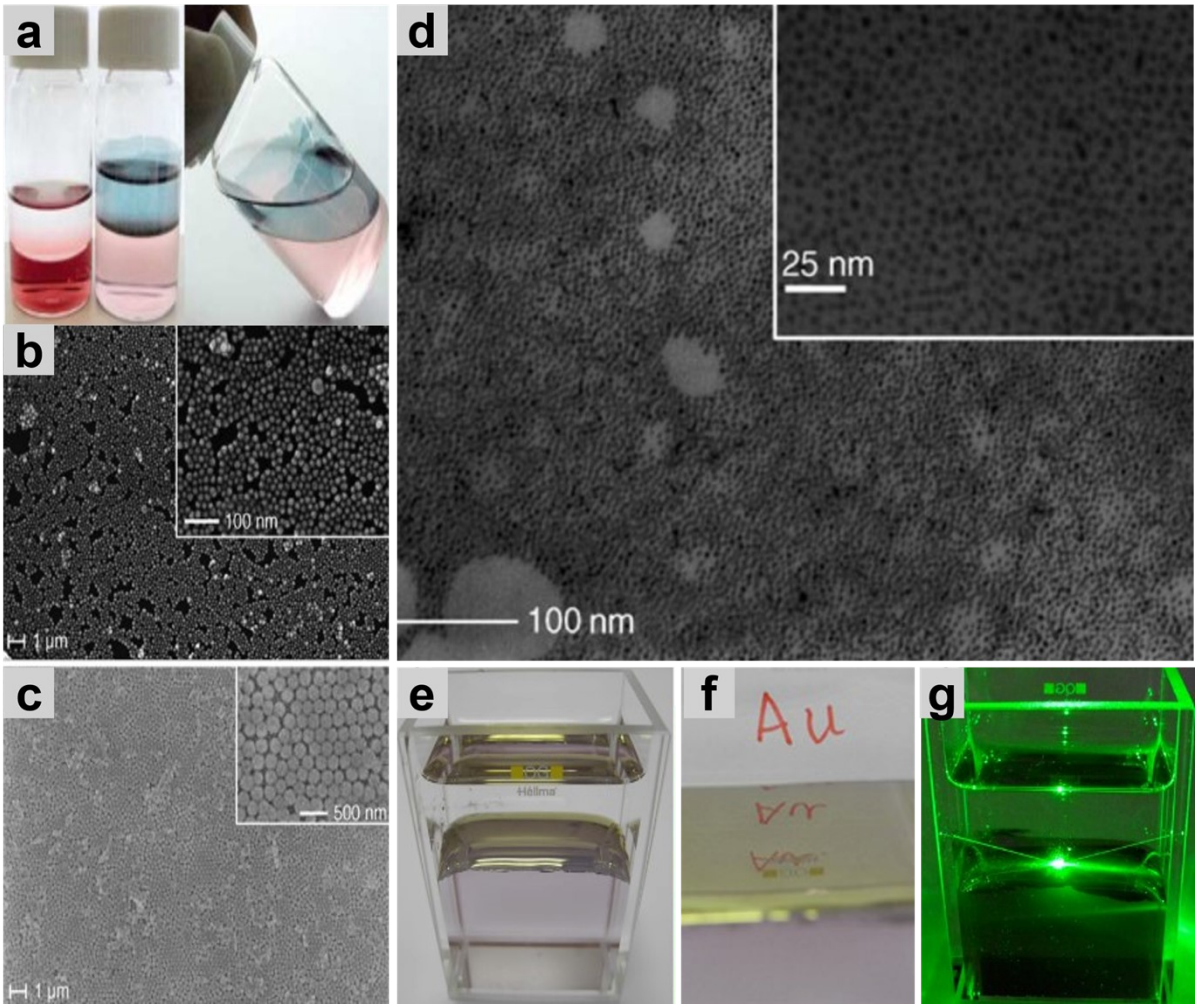

Figure S1: (a) Liquid-like assembly of citrate-covered gold nanoparticles at the water/heptane interface. In the initial stage, there is an aqueous suspension of gold nanoparticles (pink) with a layer of heptane (colorless) on top. Upon adding 4 mL of ethanol to the aqueous phase, a layer of gold nanocrystals (blue) forms at the interface of heptane and water. This layer then extends upward along the interface between heptane and glass. (a) Reproduced with permission.[1] Copyright 2004, Wiley-VCH. SEM images of multilayer films of (b) gold and (c) SiO_2 nanoparticles formed at the toluene/water interface. (d) TEM images show the formation of monolayer films of Pt and PVP at the interface between water and heptane. (b-d) Reproduced with permission.[2] Copyright 2006, Wiley-VCH. (e-g) Optical images of gold nanoparticles` films prepared at the [heptane + DCE]/water interface. (e-f) In the absence of laser light. (g) Irradiated with laser light at a wavelength of 532 nm. (e-g) Reproduced with permission. Copyright 2013.[3] American Chemical Society.

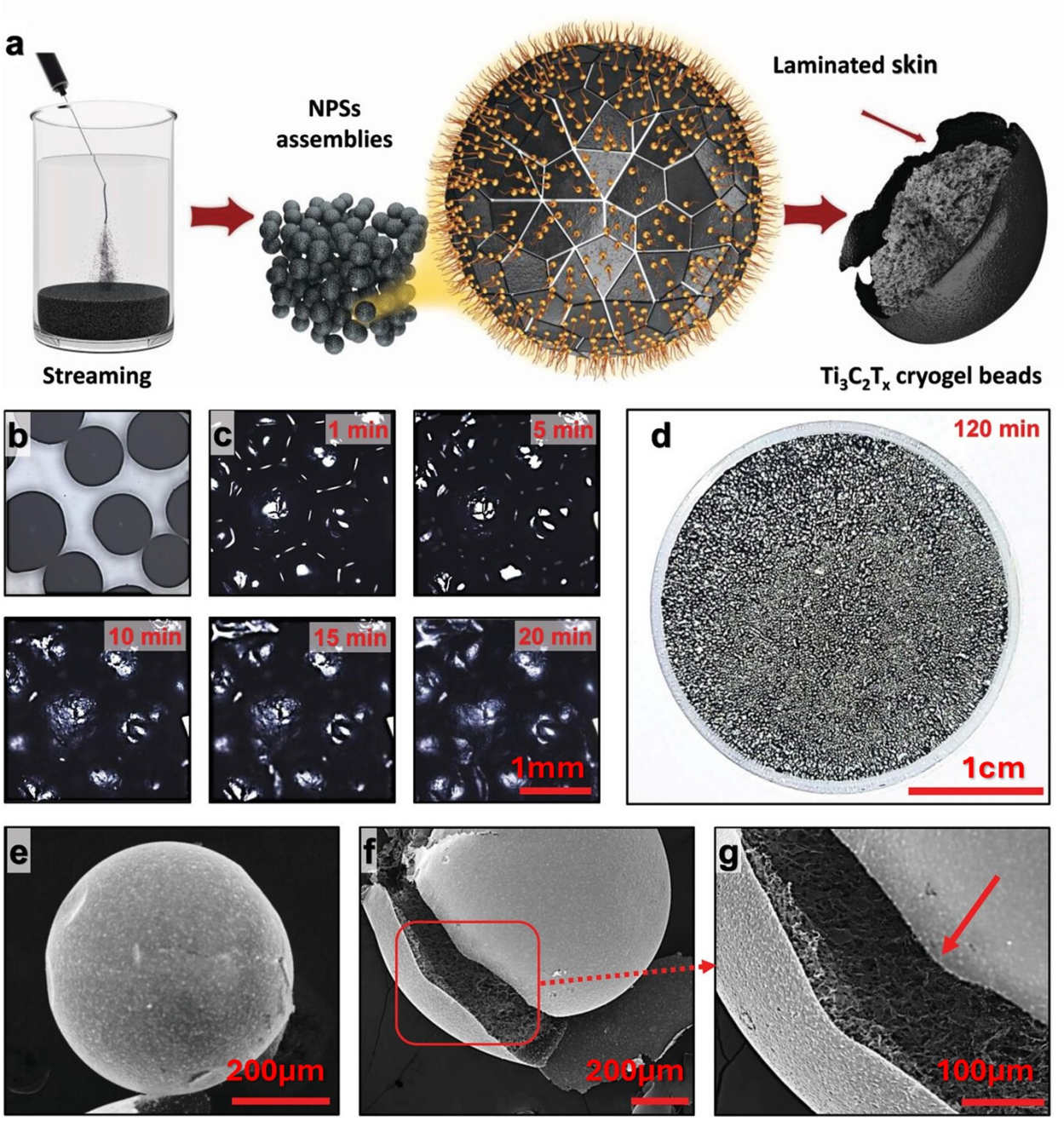

Figure S2: (a) Schematic depicting $Ti_3C_2T_x$ bead formation by injecting an aqueous $Ti_3C_2T_x$ suspension into a hexane bath with POSS as a ligand. Microscopy images of $Ti_3C_2T_x$ beads (b) pre-hexane removal and (c) post-hexane removal. (d) Digital image of $Ti_3C_2T_x$ beads taken 120 min after hexane removal. (e–g) FESEM images of freeze-dried $Ti_3C_2T_x$ aerogel beads displaying an interfacially driven skin. (a-g) Reproduced with permission.[4] Copyright 2023, Wiley-VCH.

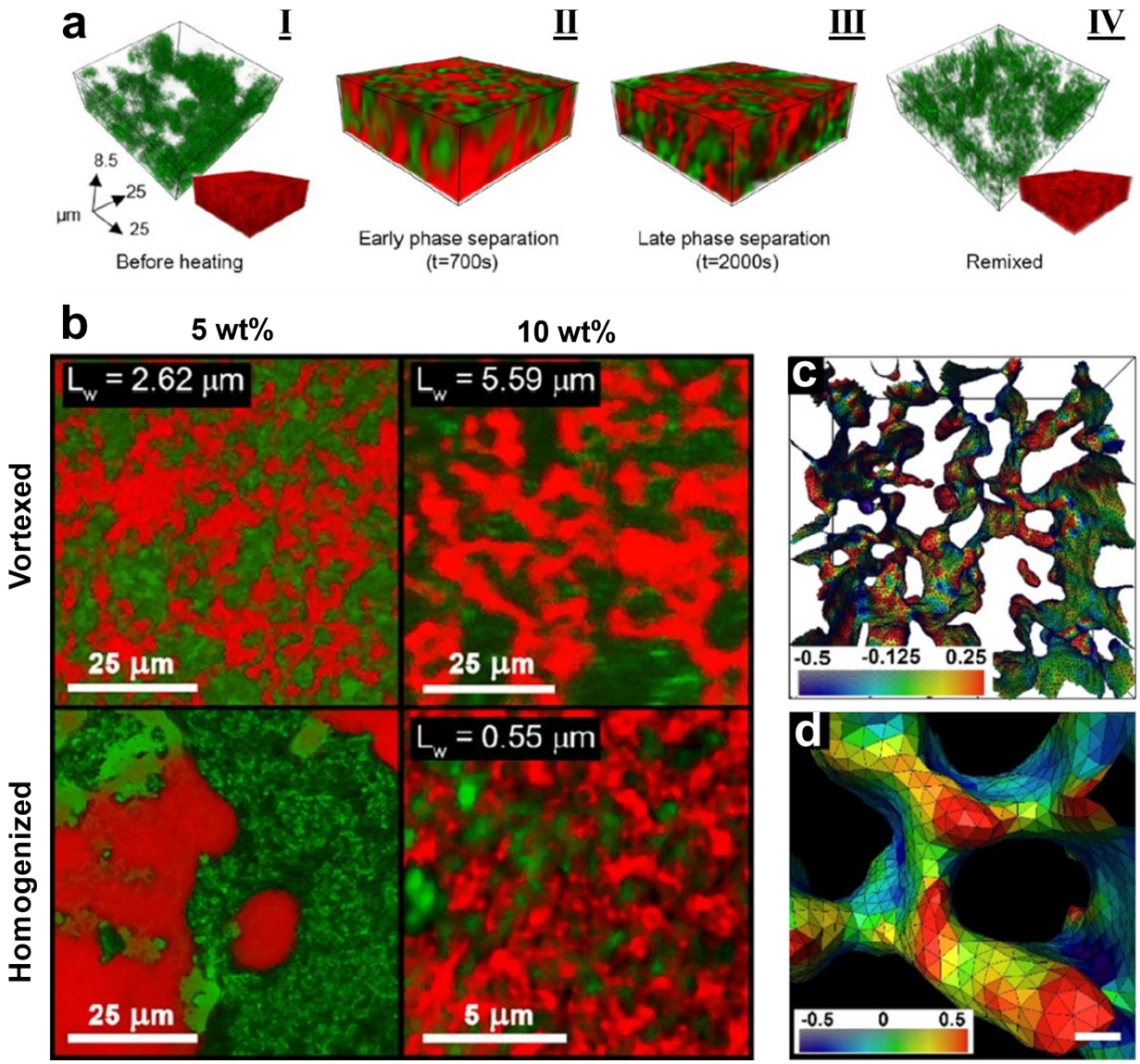

Figure S3: (a) 3D rendering of LCSM images of 5 wt% vortex mixed AlO-SiO nanoparticles in the stabilized lutidine/water system at different stages (I-IV); (I-IV) 552 nm laser reflection from the AlO-SiO nanoparticles can be seen in green, while the fluorescence backscatter of Nile red is illustrated in red, showing the lutidine phase. (b) LSCM images of bicontinuous arrangements formed with 5 and 10 wt% nanoparticles loading, either vortex mixed or homogenized; the green color shows the aqueous phase and the red one showcases the lutidine phase. (c-d) A view of the Bijel system curvature after surface reconstruction for lutidine/water system reinforced with 10 wt% nanoparticles loading. (a-d) Reproduced with permission.[5] Copyright 2019, American Chemical Society.

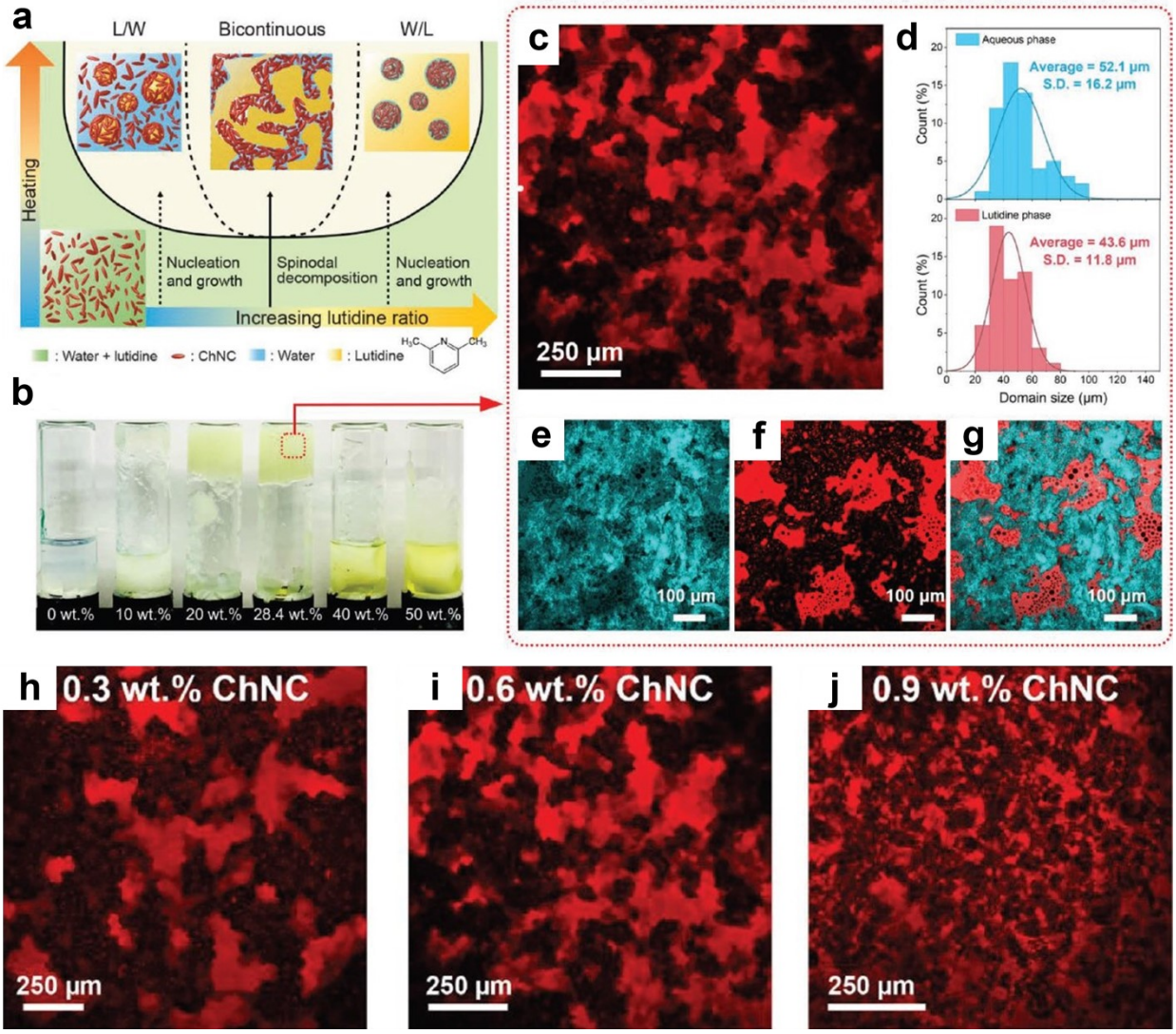

Figure S4: (a) Jammed chitin nanocrystals (cited as ChNC in the image) emulsion gel's formation, triggered via thermally induced phase separation, a transition from oil in water (O/W) or water in oil (W/O) emulsion to Bijel. (b) Formation of chitin nanocrystals jammed emulsion gel with different lutidine loadings. (c) Confocal image of chitin Bijel formed with 28.4 wt% lutidine content. (d) Domain size distribution of aqueous and lutidine phases in the bicontinuous arrangement. Florescent confocal images of the stained (e) chitin nanocrystals, (f) lutidine phase, and (g) mixture of both; the concentration of chitin nanocrystals was set at 0.6 wt%. Confocal microscope images of chitin nanocrystals Bijel at (h) 0.3 wt%, (i) 0.6 wt%, and (j) 0.9 wt% chitin nanocrystals concentrations. (a-j) Reproduced with permission.[6] Copyright 2023, Wiley-VCH.

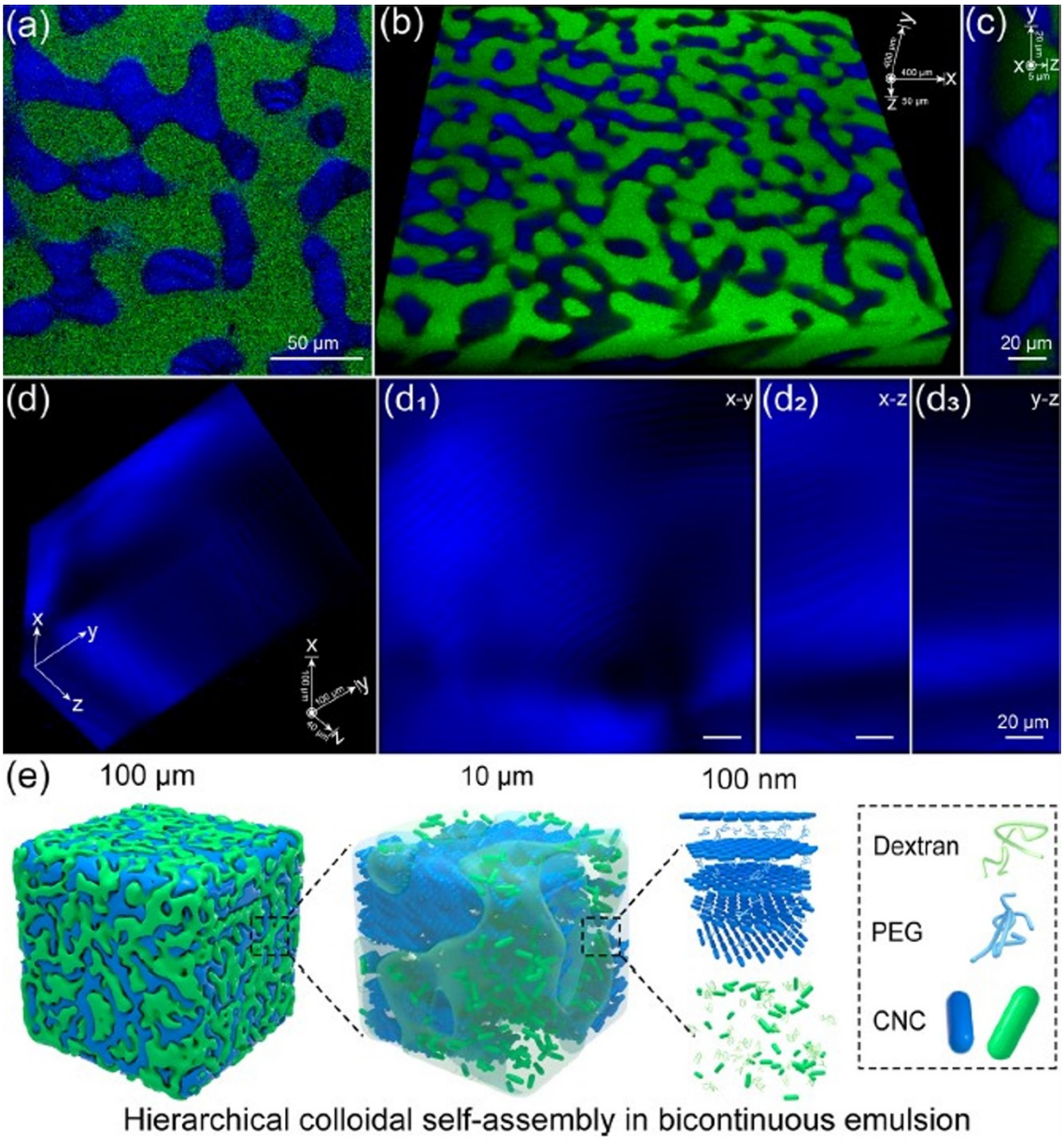

Figure S5: 3D morphology of the all-aqueous Bijel system. (a) A high-resolution LSCM image of the Bijel shows the bicontinuous arrangement of the binary dextran and polyethylene glycol domains. (b) Confocal image of the Bijel constructs showcasing the 3D arrangement. (c) Cross-sectional image of the bicontinuous arrangement. (d) Polarized LSCM image of the Bijel constructs with a specific focus on the polyethylene glycol domain, showcasing a fingerprint-shaped cholesteric domain. (d_1-d_3) Zoom on the reconstructed focus planes of the LSCM image in (d). (e) Formation of a hierarchical bicontinuous arrangement upon self-assembly of cellulose nanocrystals in the Bijel system. (a-e) Reproduced with permission.[7] Copyright 2022, American Chemical Society.

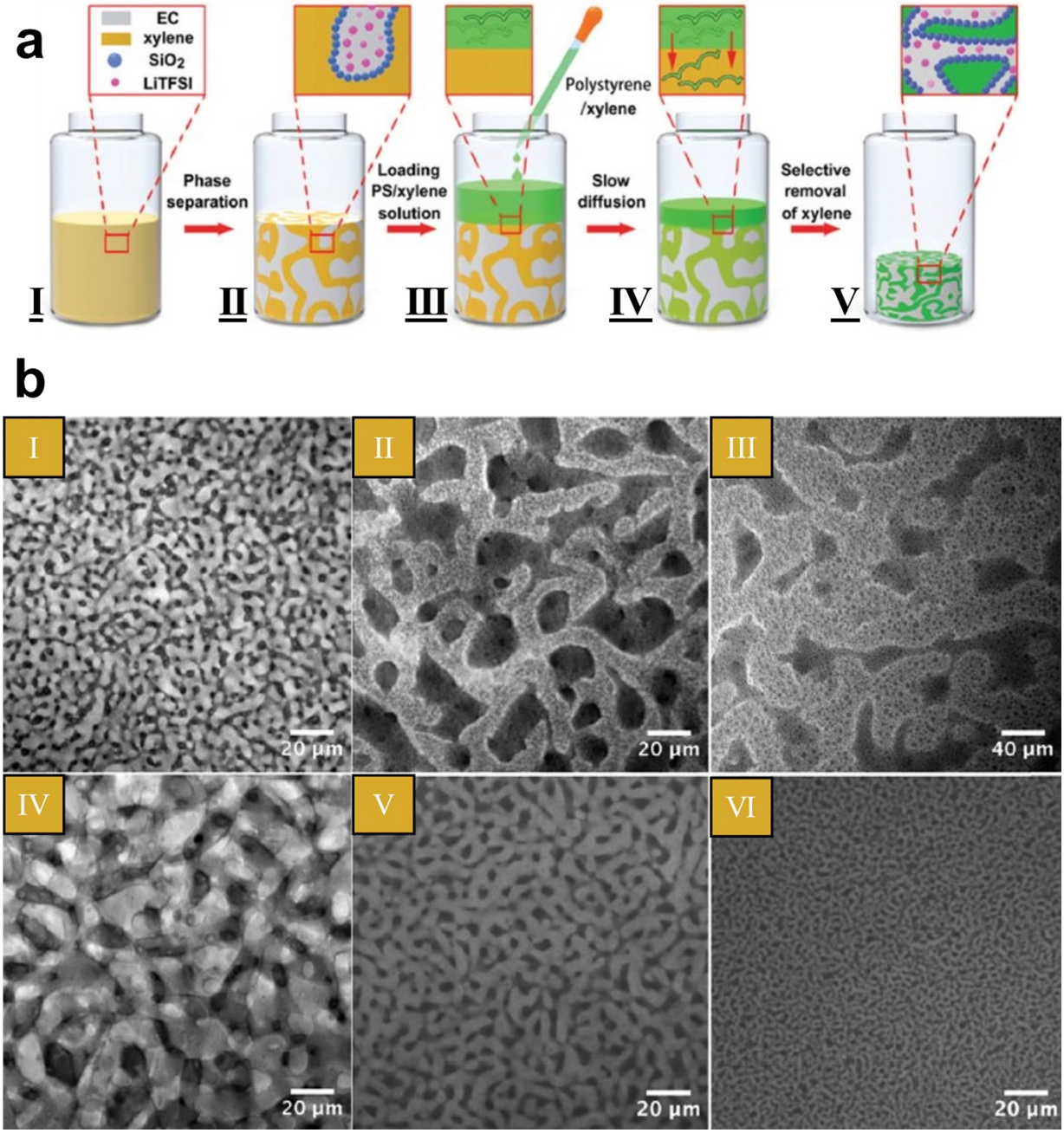

Figure S6: (a) Schematic illustration of the methodology for generating a bicontinuous electrolyte system: (I) single fluid phase consisted of ethylene carbonate, LiTFSI enriched xylene, and silica nanoparticles, (II) arrested spinodal decomposition of the ethylene carbonate and xylene upon thermal quenching, (III) adding the polystyrene/xylene solution to the Bijel, (IV) selective polystyrene diffusion in the xylene phase, and (V) selective xylene removal toward polystyrene phase solidification. (b) Confocal images of the spinodal decomposition, arrested by

the proposed bicontinuous system; (I-III) locked spinodal decomposition by 2.6 vol% particles (ratio of hexamethyldisilazane (HMDS) over particles was 0.4) in which sample in parts (II) and (III) were filled with 0.1 and 0.3 M LiTFSI, respectively. (IV-VI) Confocal images of the Bijel system with 0.1 M LiTFSI in ethylene carbonate stabilized via 0.6, 1.8, and 3.6 vol% particles, respectively (ratio of HMDS over particles was 0.16). (a-b) Reproduced with permission.[8] Copyright 2018, Royal Society of Chemistry.

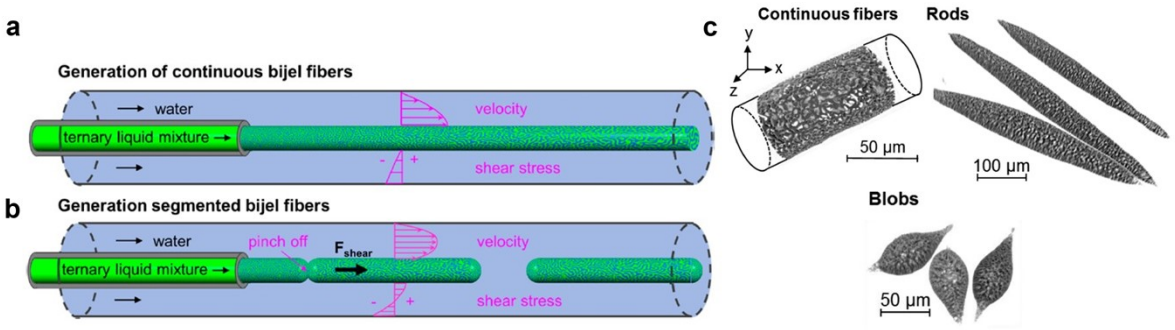

Figure S7: Formation of Bijel (a) fibers and (b) customized segments via STRIPS method. (c) Confocal micrograph from 3D structured Bijel threads, rods, and blobs. In this image, the dark and bright areas represent the oil and water phases, respectively. (a-c) Reproduced with Permission.[9] Copyright 2016, American Chemical Society.

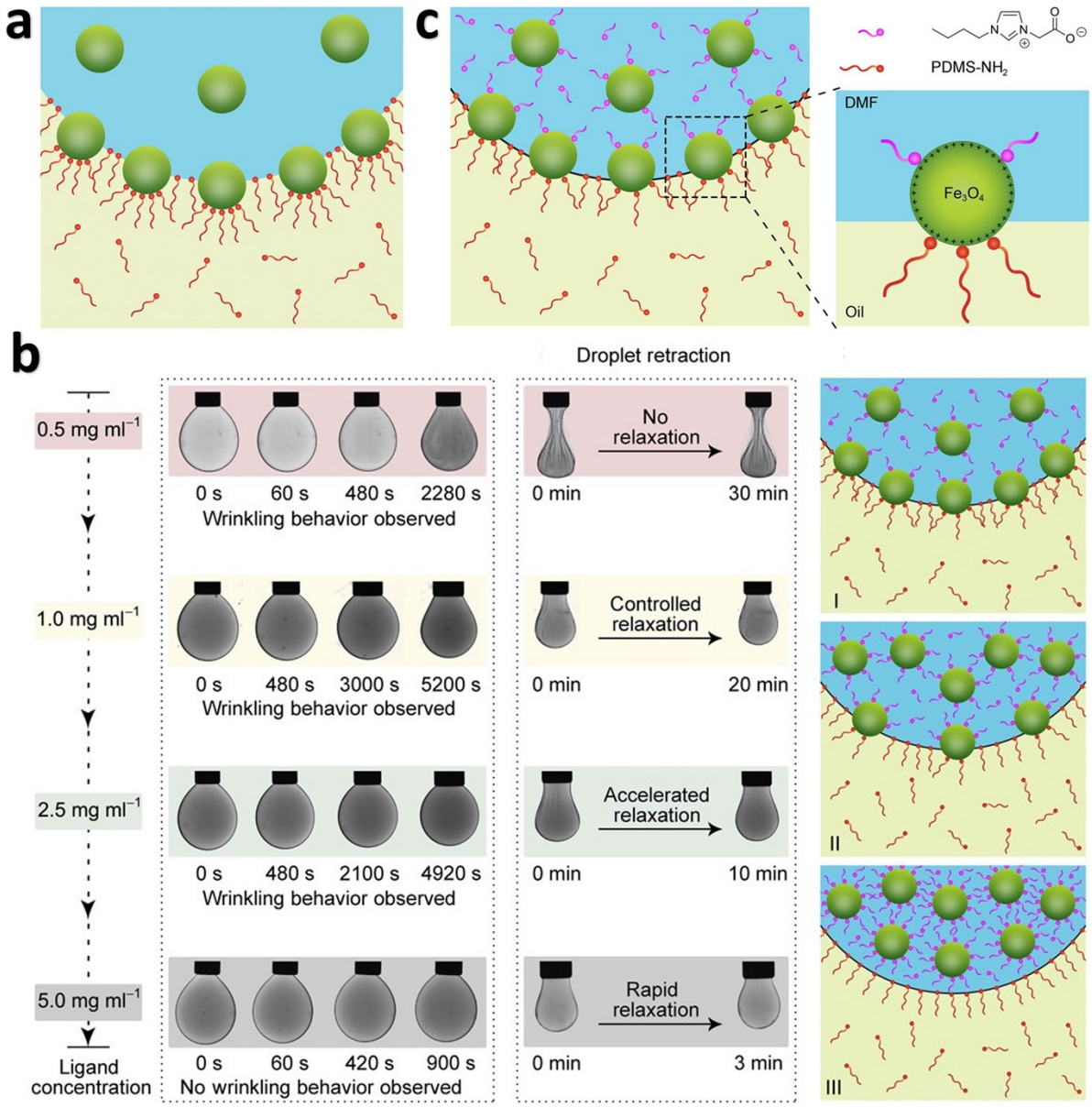

Figure S8: (a) The interfacial interaction between a cationic/Lewis acidic dispersion of Fe_3O_4 in N, N-dimethylformamide (DMF), and a complementary Lewis basic PDMS-NH_2 in PDMS oil. This system is described by the irreversible and solid-like assembly of NPSs at the liquid-liquid interface. (a-b) Upon the addition of a competitive zwitterionic ligand, i.e., 2-(3-butyl-1H-imidazol-3-ium-1-yl)acetate, to DMF, the system showcases liquid-like behavior at the interface, as evident in the contraction and relaxation test of a pendant drop. (a-c) Reproduced with permission.[10] Copyright 2018, American Association for the Advancement of Science.

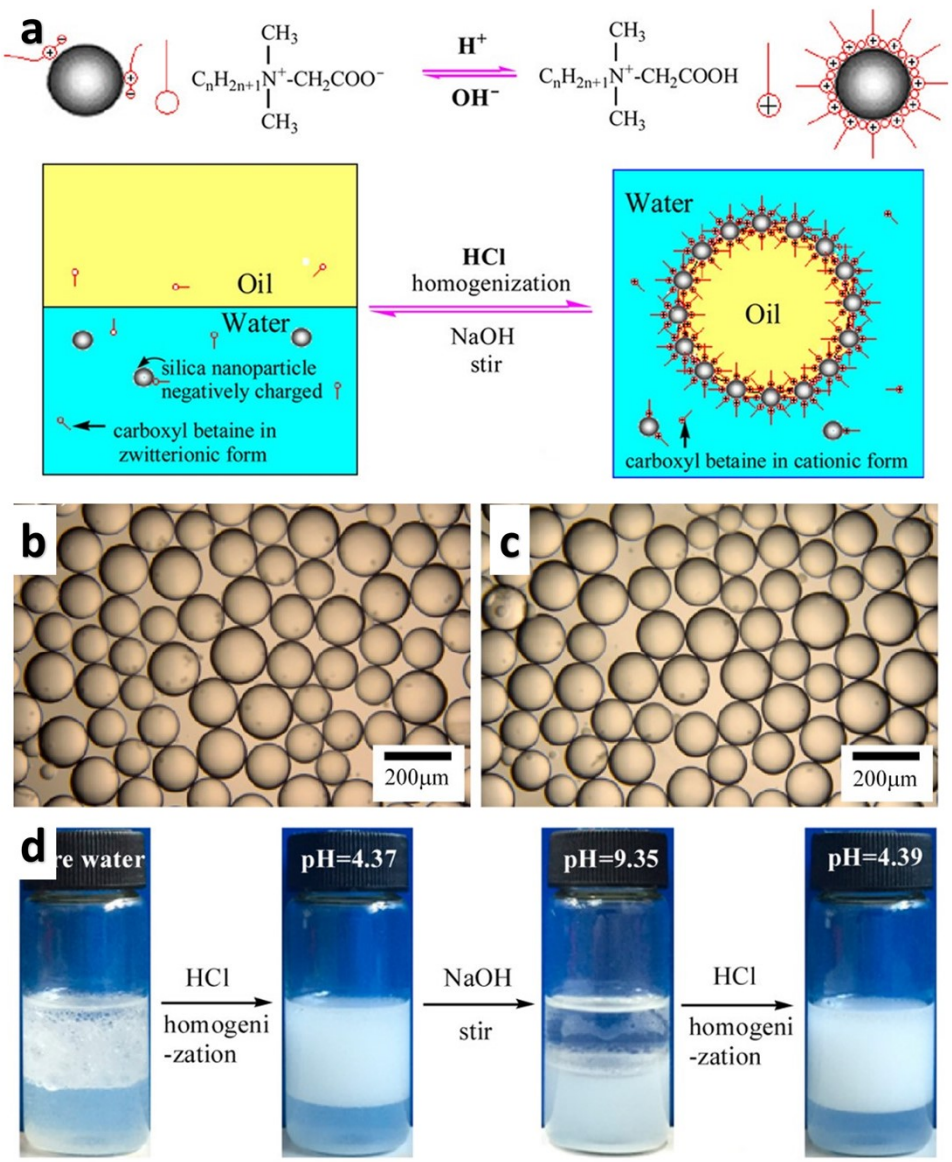

Figure S9: (a) pH-responsive oil-in-water Pickering emulsions containing negatively charged SiO_2 nanoparticles and a zwitterionic carboxyl betaine surfactant as a stabilizer. Optical micrographs depict decane-in-water emulsions containing 0.5 wt % silica nanoparticles and 0.06 mM zwitterionic carboxyl betaine surfactant at a pH of approximately 4.3 after (b) 24 hours and (c) 3 months. (d) In acidic conditions, the ligand assumes a cationic state, adsorbing onto SiO_2 nanoparticles to stabilize the emulsions. However, as the pH exceeds 8.5, the ligands undergo a conversion to the zwitterionic state and subsequently desorb from the surfaces of the nanoparticles, leading to demulsification. (a-d) Reproduced with permission.[11] Copyright 2017, American Chemical Society.

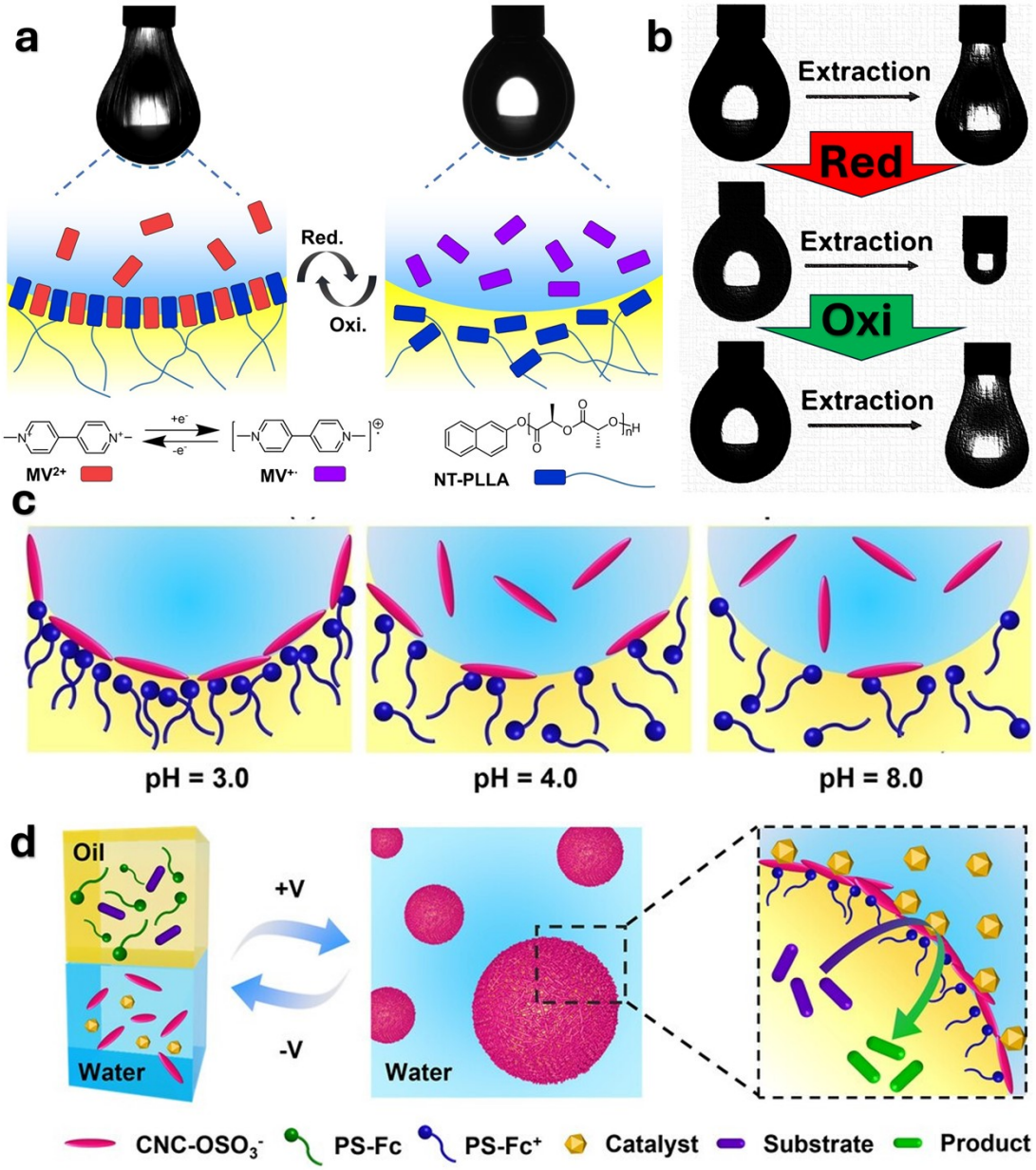

Figure S10: (a) Redox-responsive structured liquids based on methyl viologen (MV^{2+} dissolved in water) and naphthalene-terminated poly-L-lactic acid (NT-PLLA dissolved in toluene). (b) Upon the reduction of MV^{2+} with $Na_2S_2O_4$, the interfacial assembly and jamming of NPS at the liquid-liquid interface diminish, and no visible wrinkles are observed upon contraction of the pendant drop. (a-b) Reproduced with permission.[12] Copyright 2021, Wiley-VCH. (c) The structured liquid that forms through electrostatic interactions between sulfated CNC (CNC-OSO_3^-) and ferrocenium-terminated polystyrene (PS-Fc^+) at the oil/water interface is responsive to (c) pH and (d) voltage. (c-d) Reproduced with permission.[13] Copyright 2023, Wiley-VCH.

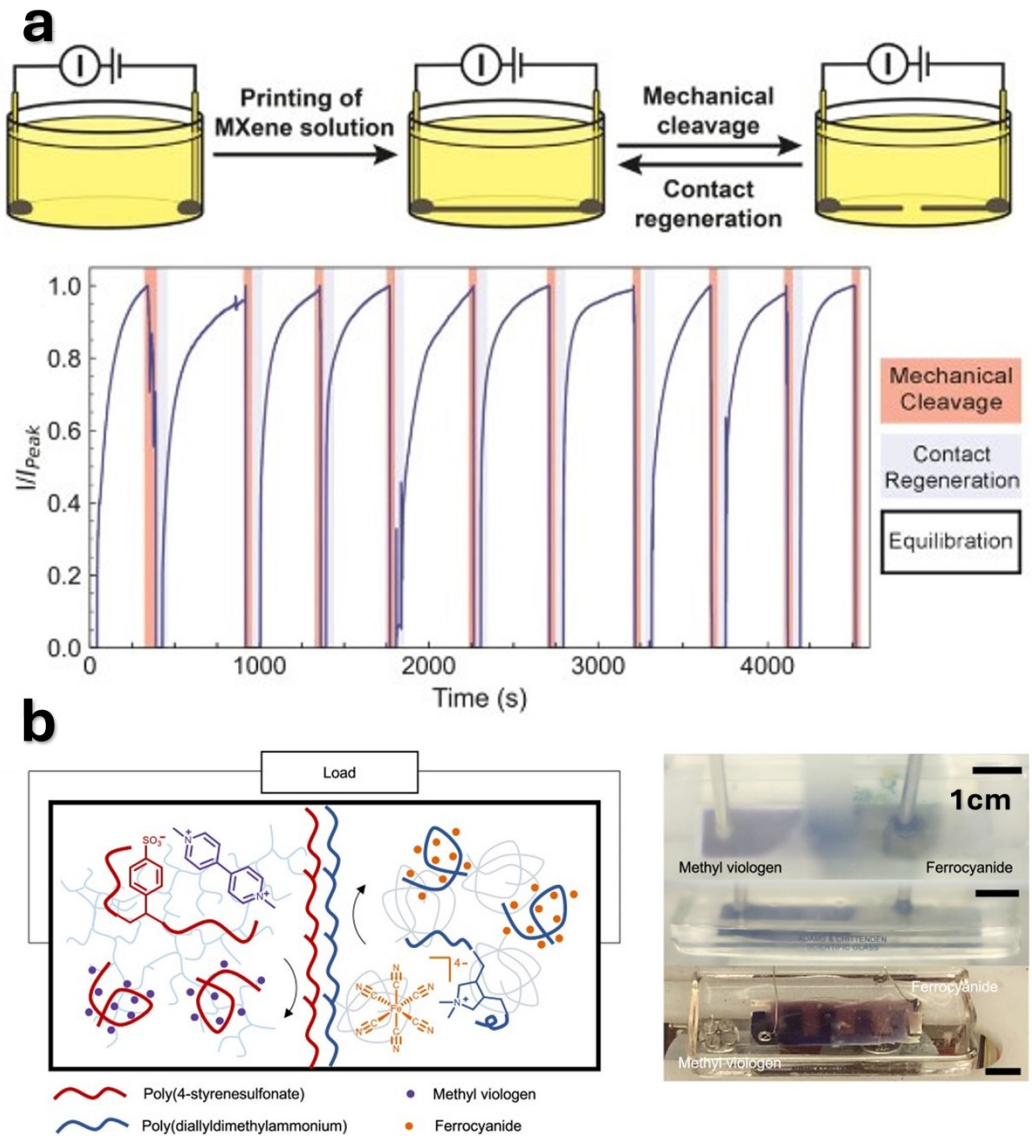

Figure S11: (a) A structured aqueous stream of MXene demonstrates versatile functionality as an all-liquid on-off switch. Here, the liquid threads conduct electricity, and the connection can be cut off simply by cleaving the MXene thread. This thread can then be reconfigured back to its original state by adding a few droplets of MXene aqueous suspension, which heals the disconnected section. (a) Reproduced with permission.[14] Copyright 2023, Wiley-VCH. (b) All-liquid batteries were fabricated through interfacial assembly of polyelectrolytes. In this system, interfacial assembly was achieved in a biphasic system containing two aqueous phases: one containing dextran and poly(sodium 4-styrenesulfonate) (PSS−Na), and the other containing

poly(ethylene glycol) (PEG) and poly(diallyldimethylammonium chloride) (PDADMA−Cl). (b) Reproduced with permission.[15] Copyright 2022, American Chemical Society.

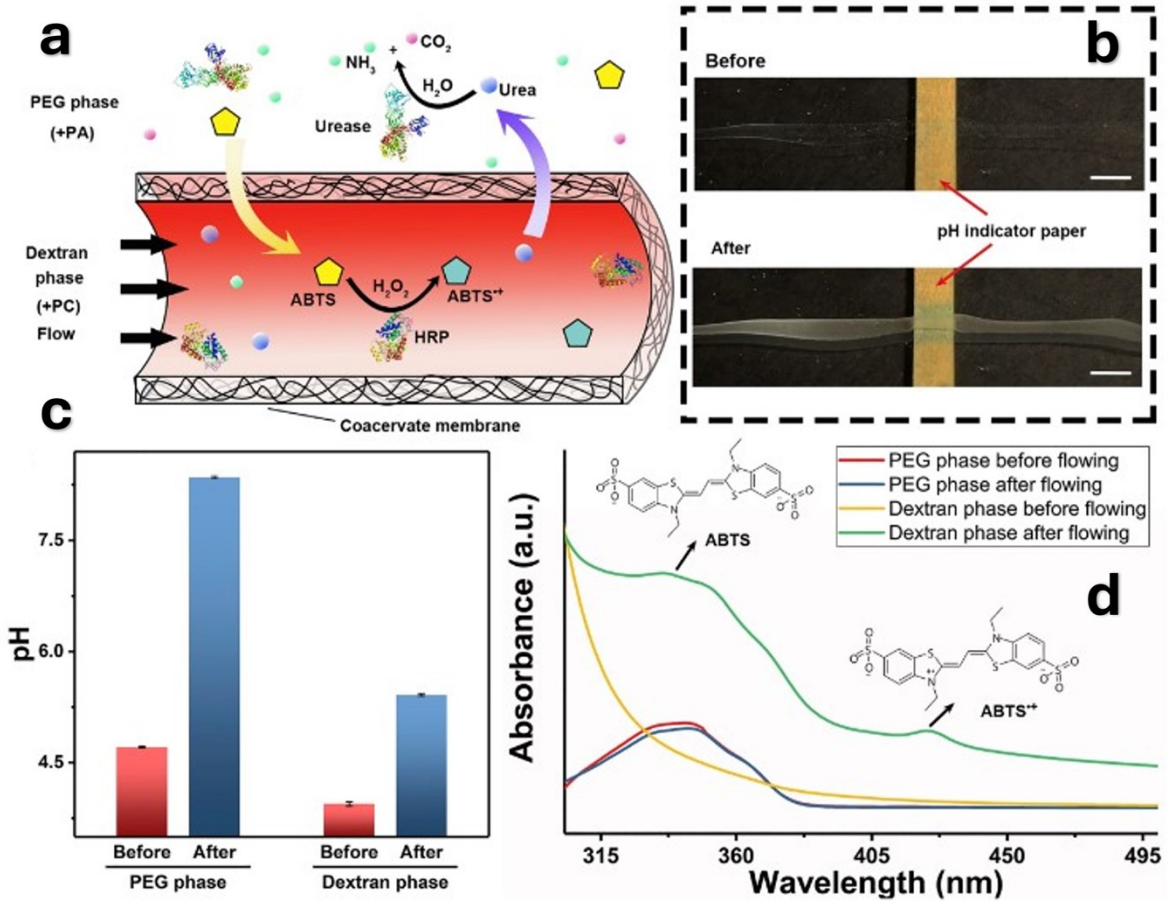

Figure S12: (a) Continuous compartmentalized reactions can be performed in all aqueous microfluidic devices. In this scenario, an aqueous suspension of dextran containing urea, HRP enzyme, and H_2O_2 is directed through the printed microchannels, while urease and 2,20-azino-bis(3-ethylbenzothiazoline-6-sulphonic acid) diammonium salt (ABTS) are added to the external PEG bath. (b-c) In the first reaction, urease catalyzes the hydrolysis of urea into carbon dioxide and ammonia. To validate this reaction, the pH values of both aqueous phases were monitored during the reaction. The pH of the PEG phase increases from 4 to 8.5 after continuous urea hydrolysis for 1 hour, and the pH in the dextran phase increases with a smaller magnitude due to the diffusion of ammonia. (d) In the second reaction, ABTS was oxidized into $ABTS^+$ by H_2O_2 as the oxidizing agent and horseradish peroxidase (HRP) as the catalyst. In this scenario, the 415 nm peak from $ABTS^+$ in the ultraviolet-visible (UV-vis) spectrum is only detected in the dextran

solution and not in the PEG phase, confirming the compartmentalized reactions. (a-d) Reproduced with permission.[16] copyright Elsevier 2019.

References

1. F. Reincke, S. G. Hickey, W. K. Kegel and D. Vanmaekelbergh, *Angewandte Chemie-International Edition*, 2004, **43**, 458-462.
2. Y. J. Li, W. J. Huang and S. G. Sun, *Angew. Chem. Int. Ed.*, 2006, **45**, 2537-2539.
3. P.-P. Fang, S. Chen, H. Deng, M. D. Scanlon, F. Gumy, H. J. Lee, D. Momotenko, V. Amstutz, F. Cortés-Salazar and C. M. Pereira, *ACS nano*, 2013, **7**, 9241-9248.
4. A. Ghaffarkhah, S. A. Hashemi, S. Rostami, M. Amini, F. Ahmadijokani, A. Pournaghshband Isfahani, S. E. Mhatre, O. J. Rojas, M. Kamkar and S. Wuttke, *Adv. Funct. Mater.*, 2023, **33**, 2304748.
5. B. Kinkead, R. Malone, G. Smith, A. Pandey and M. Trifkovic, *Chemistry of Materials*, 2019, **31**, 7601-7607.
6. Y. Lu, M. Kamkar, S. Guo, X. Niu, Z. Wan, J. Xu, X. Su, Y. Fan, L. Bai and O. J. Rojas, *Small*, 2023, **19**, 2300686.
7. S. Guo, H. Tao, G. Gao, S. Mhatre, Y. Lu, A. Takagi, J. Li, L. Mo, O. J. Rojas and G. Chu, *Biomacromolecules*, 2022, **24**, 367-376.
8. D. Cai, F. H. Richter, J. H. Thijssen, P. G. Bruce and P. S. Clegg, *Materials Horizons*, 2018, **5**, 499-505.
9. M. F. Haase, N. Sharifi-Mood, D. Lee and K. J. Stebe, *ACS nano*, 2016, **10**, 6338-6344.
10. Z. Zhang, Y. Jiang, C. Huang, Y. Chai, E. Goldfine, F. Liu, W. Feng, J. Forth, T. E. Williams and P. D. Ashby, *Sci. Adv.*, 2018, **4**, eaap8045.
11. K. Liu, J. Jiang, Z. Cui and B. P. Binks, *Langmuir*, 2017, **33**, 2296-2305.
12. S. Sun, C. Xie, J. Chen, Y. Yang, H. Li, T. P. Russell and S. Shi, *Angew. Chem. Int. Ed.*, 2021, **60**, 26363-26367.
13. Y. Yang, H. Sun, M. Wang, M. Li, Z. Zhang, T. P. Russell and S. Shi, *Angew. Chem. Int. Ed.*, 2023, **62**, e202218440.
14. D. Popple, M. Shekhirev, C. Dai, P. Kim, K. X. Wang, P. Ashby, B. A. Helms, Y. Gogotsi, T. P. Russell and A. Zettl, *Adv. Mater.*, 2023, **35**, 2208148.
15. J. Yan, M. A. Baird, D. C. Popple, A. Zettl, T. P. Russell and B. A. Helms, *J. Am. Chem. Soc.*, 2022, **144**, 3979-3988.
16. G. Xie, J. Forth, Y. Chai, P. D. Ashby, B. A. Helms and T. P. Russell, *Chem*, 2019, **5**, 2678-2690.